



52nd SME North American Manufacturing Research Conference (NAMRC 52, 2024)

Analytical temperature model for spindle speed selection in additive friction stir deposition

Tony Schmitz^{1,2*}, Elijah Charles¹, and Brett Compton¹

¹University of Tennessee, Knoxville, Knoxville, TN

²Manufacturing Demonstration Facility, Oak Ridge National Laboratory, Knoxville, TN

*Tony Schmitz. Tel.: +1-865-974-6141; E-mail address: tony.schmitz@utk.edu

Abstract

This paper describes a physics-based, analytical model for additive friction stir deposition (AFSD) spindle speed selection to achieve a desired deposition temperature. In the model, power input to the feedstock, which enables plastic flow and deposition, is related to the material temperature rise and subsequent flow stress reduction using Fourier's conduction rate equation. Power input is modeled as frictional heating at the deposit-surface interface and adiabatic heating due to plastic deformation. The flow stress is predicted using the strain, strain rate, and temperature-dependent Johnson-Cook constitutive model for the selected feedstock alloy. Model predictions are compared to AFSD numerical simulation results available in the literature and experiments for aluminum alloys.

© 2024 The Authors. Published by ELSEVIER Ltd. This is an open access article under the CC BY-NC-ND license (<https://creativecommons.org/licenses/by-nc-nd/4.0>)

Peer-review under responsibility of the scientific committee of the NAMRI/SME.

Keywords: Additive manufacturing; additive friction stir deposition; temperature

1. Introduction

Additive friction stir deposition (AFSD) is a solid-state additive manufacturing (AM) process that provides an alternative to beam-based AM processes which melt the material locally to obtain the desired near-net shape geometry [1-4]. Important applications for AFSD include part repair [5] and preform production for castings, forgings, spare parts, and parts with short delivery times [6]. AFSD provides fully dense materials with prescribed microstructure and properties using process parameter selection and in situ control [7]. Prior research efforts have studied the AFSD property-parameter-microstructure relationships [8-17].

AFSD accomplishes solid-state deposition through plastic deformation of a square cross-section, ductile metal alloy feedstock. A tool-spindle assembly containing a square bore constrains the feedstock as it is fed axially through the spindle

and rotated against the build plate or previous layers. Spindle rotation provides heat generation through friction between the deposit and build surface and, subsequently, a reduction in the required flow stress. The feedstock is deposited during movement of the tool at the selected tool feed velocity along the prescribed motion path. The feedstock feed velocity through the tool-spindle is also specified. The combined tool rotation and feed kinematics enable layers to be bonded to the build plate and previous layers to deposit the desired preform geometry; see Fig. 1. The preform is then measured machined to obtain the final geometry and surface finish [18-22].

While the advantages of AFSD are well-documented, process parameter selection is currently based on prior experience or trial and error. The research objective for this paper is to provide a physics-based model for AFSD spindle

speed selection to achieve a desired deposition temperature. An analytical approach is selected to enable implementation with low computational expense. Deposition temperature is critical because it affects the final mechanical properties. Therefore, an approach to select spindle speed to reach a specific temperature is necessary. This effort is complementary to the finite volume method simulations reported in [23–24]. In [23], an open-source computational fluid dynamics code was used to numerically model the viscoplastic material behavior during deposition due to: 1) process heating within the material and at the tool-material interface; and 2) heat loss to the substrate and atmosphere. In [24], a computational fluid dynamics (CFD) approach is implemented where conservation of mass and momentum are used to predict the velocity distribution within the deposit, while conservation of energy is simultaneously applied to predict temperature distribution. The two distributions are solved iteratively until the solution converges.

The paper is organized as follows. Section 2 defines the analytical spindle speed-temperature model. Section 3 describes the experimental setup. Section 4 presents results and Section 5 draws conclusions.

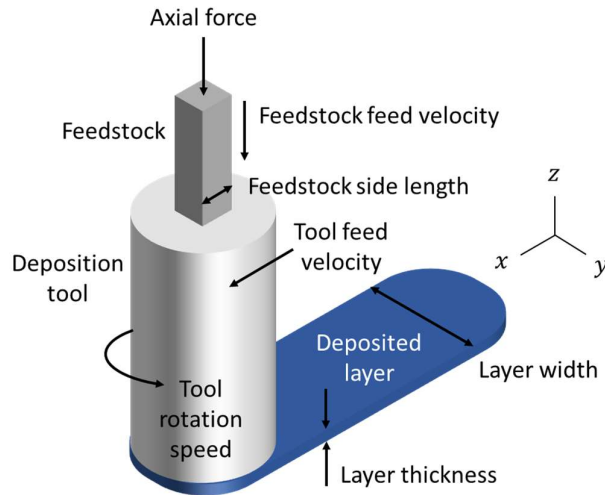


Figure 1: AFSD description.

2. AFSD Temperature Model

In this study, power input to the feedstock (to enable plastic flow and deposition) is related to the material temperature rise, and subsequent flow stress reduction, using Fourier's conduction rate equation. The assumption is that conduction dominates AFSD heat transfer; convection and radiation are neglected in this analysis. Equation 1 provides the relationship between power, P , area under the circular deposition tool, A , thermal conductivity, k , deposition temperature, T , initial temperature, T_0 , and layer thickness, h . Note that the thermal conductivity is temperature-dependent, in general. The deposition geometry is displayed in Fig. 2.

$$\frac{P}{A} = k \frac{(T - T_0)}{h} \quad (1)$$

Power input is provided by two AFSD sources: 1) frictional heating between the rotating deposit and deposition surface;

and 2) adiabatic heating due to plastic deformation of the feedstock. The friction power, P_f , is calculated using Eq. 2, where T_f is the torque required to overcome the friction force, F_f , and ω is the tool rotating speed (spindle speed). The torque is rewritten in Eq. 2 as a product of the friction force and radius at which the friction force acts, r_f . Assuming dry sliding friction, the friction force is rewritten as the product of the normal force in the axial (z) direction, F_z , between the rotating deposit and deposition surface and the Coulomb friction coefficient, μ . Finally, the normal force is replaced by the product of the flow stress, σ , and the deposit area.

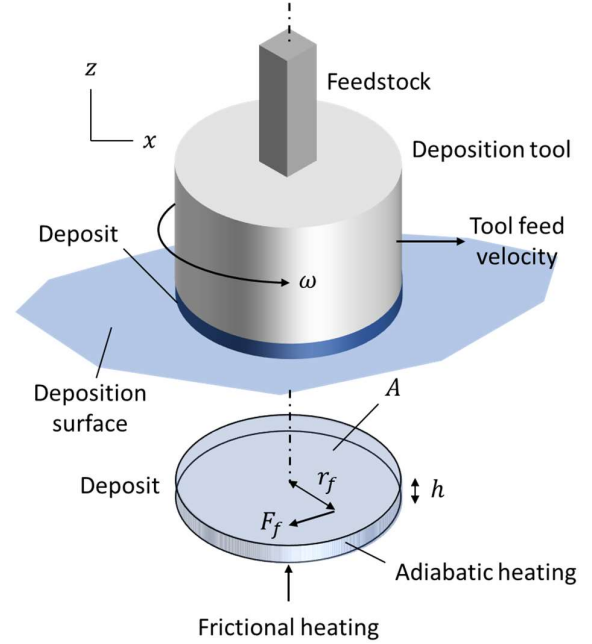


Figure 2: AFSD deposition geometry.

$$P_f = T_f \omega = F_f r_f \omega = \mu F_z r_f \omega = \mu \sigma A r_f \omega \quad (2)$$

The flow stress in Eq. 2 is predicted using the strain, strain rate, and temperature-dependent Johnson-Cook flow stress model provided in Eq. 3, where ϵ is the equivalent plastic strain, $\dot{\epsilon}_e$ is the effective (plastic) strain rate, $\dot{\epsilon}_0$ is the reference strain rate, T_m is the feedstock melting temperature, and A , B , C , n , and m are model parameters obtained from experiments for the selected feedstock material.

$$\sigma = (A + B \epsilon^n) \left(1 + C \ln \frac{\dot{\epsilon}_e}{\dot{\epsilon}_0}\right) \left(1 - \left(\frac{T - T_0}{T_m - T_0}\right)^m\right) \quad (3)$$

The equivalent plastic strain is modeled after forward extrusion in metal forming [25], where the true strain is calculated using the initial cross-sectional area, A_0 , and extruded cross-sectional area, A_1 . This strain is shown in Eq. 4 for the AFSD geometry, where the initial area is calculated using the square feedstock side length, s , and the extruded area is the perimeter (assumed circular) at the friction radius multiplied by the deposition layer thickness.

$$\epsilon = -\ln \frac{A_0}{A_1} = -\ln \frac{s^2}{2\pi r_f h} \quad (4)$$

The effective strain rate for Eq. 3 is calculated using the kinematics of the rotating-translating deposition tool motion, the gradient of velocity, L , the strain rate tensor, E , and the strain rate, $\dot{\epsilon}$. The tool feed velocity, f , occurs in the x direction and the rotation direction is counterclockwise for the deposition tool; see Fig. 3, where the u and v velocity components are also shown. The associated displacement and velocity expressions are given in Eqs. 5-8, where ϕ is the time-dependent tool rotation angle.

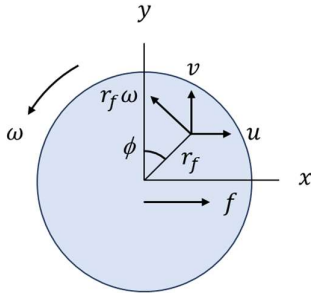


Figure 3: Rotating-translating deposition tool kinematics. Spindle rotation is counter-clockwise and tool feed velocity is to the right.

$$x(t) = r_f \sin \phi + ft \quad (5)$$

$$y(t) = r_f \cos \phi \quad (6)$$

$$u(t) = -r_f \omega \cos \phi + f \quad (7)$$

$$v(t) = r_f \omega \sin \phi \quad (8)$$

The two-dimensional gradient of velocity is defined in Eq. 9, where the individual terms in the ratios are calculated by numerical differentiation of Eqs. 5-8. The strain rate tensor is calculated using Eq. 10, where T is the transpose operator.

$$L = \begin{bmatrix} \frac{du}{dx} & \frac{du}{dy} \\ \frac{dv}{dx} & \frac{dv}{dy} \end{bmatrix} \quad (9)$$

$$E = \frac{1}{2}(L + L^T) = \begin{bmatrix} \frac{du}{dx} & \frac{1}{2}\left(\frac{du}{dy} + \frac{dv}{dx}\right) \\ \frac{1}{2}\left(\frac{du}{dy} + \frac{dv}{dx}\right) & \frac{dv}{dy} \end{bmatrix} \quad (10)$$

The strain rate is determined using Eq. 11, where $\langle E, E \rangle$ represents the inner product. Finally, the effective strain rate is calculated using the mean value of Eq. 11 for one tool revolution (i.e., ϕ is varied from 0 to 2π rad in Eqs. 5-8 and the mean value is determined).

$$\dot{\epsilon} = \left(\frac{2}{3} \langle E, E \rangle \right)^{\frac{1}{2}} = \left(\frac{2}{3} (E_{11}^2 + E_{12}^2 + E_{21}^2 + E_{22}^2) \right)^{\frac{1}{2}} \quad (11)$$

The adiabatic power, P_a , due to plastic deformation is calculated using Eq. 12, where the Taylor-Quinney coefficient [26-27], or ratio of dissipated heat to plastic work, is taken to be 0.9 for this study.

$$P_a = 0.9\sigma\dot{\epsilon}_e Ah \quad (12)$$

Substitution of Eqs. 2 and 12 into Eq. 1 provides a relationship between temperature and spindle speed, where it is noted that the flow stress depends on the effective strain rate and, therefore, the spindle speed.

$$\frac{\mu\sigma A r_f \omega + 0.9\sigma\dot{\epsilon}_e Ah}{A} = k \frac{(T - T_0)}{h} \quad (13)$$

Solving Eq. 13 for the spindle speed provides an analytical solution for spindle speed selection based on the desired deposition temperature and feedstock material. Inputs include the Johnson-Cook flow stress model parameters, temperature-dependent thermal conductivity, layer thickness, tool feed velocity, friction radius, and friction coefficient.

$$\omega = \frac{k(T - T_0) - 0.9\sigma\dot{\epsilon}_e h^2}{\mu\sigma r_f h} \quad (14)$$

The relationship between deposition temperature and spindle speed is established using the following steps:

1. select the desired deposition temperature
2. determine the temperature-dependent thermal conductivity from available data
3. calculate the effective strain rate for a pre-selected spindle speed range using the mean value of Eq. 11 for one tool revolution
4. calculate the flow stress over the same spindle speed range from step 3 using Eq. 3
5. evaluate the spindle speed-dependent test function obtained by rewriting Eq. 14, $f(\omega) = k(T - T_0) - 0.9\sigma\dot{\epsilon}_e h^2 - \mu\sigma r_f h \omega = 0$, over the same spindle speed range as steps 3 and 4
6. determine the zero crossing for $f(\omega)$ and identify the corresponding spindle speed
7. record the spindle speed for the selected deposition temperature
8. repeat steps 1-7 for the next deposition temperature.

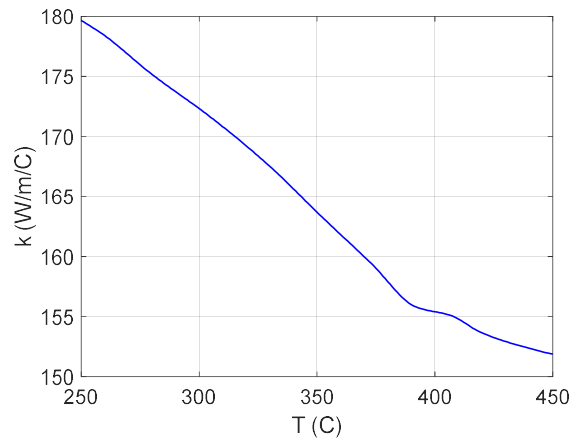


Figure 4: Temperature-dependent thermal conductivity for 7075-T651 aluminum [35].

To demonstrate the algorithm, results are presented for 6061 aluminum feedstock with comparison to the finite volume simulation results described in [23]. The 6061 aluminum

Johnson-Cook flow stress model parameters are provided in Table 1 from multiple sources [28-35], the temperature-dependent thermal conductivity is displayed in Fig. 4 [36] for a similar aluminum alloy, the tool feed velocity is 126 mm/min, the layer thickness is 1.5 mm, the friction radius is 9.525 mm (selected to be half the deposition tool radius of 19.05 mm), the friction coefficient is 0.25 (representative of elevated temperature forming conditions in traditional metalworking [25]), the initial temperature is 25 °C, and the square feedstock side length is 9.525 mm.

Table 1: Johnson-Cook model parameters for 6061 aluminum [27-34]. All reference strain rate values are 1 (1/s). All melting temperatures are 652 C.

Model	A (MPa)	B (MPa)	C	n	m	Reference
1	250	79.7	0.0249	0.499	1.499	27
2	293.4	121.2	0.002	0.23	1.34	28
3	324.1	113.8	0.002	0.42	1.34	29
4	250	70	0.001	0.499	1	30
5	250	70	0.001	0.499	1.315	30
6	250	137	0.0205	0.499	1.499	30
7	250	209	0.001	0.499	1.499	30
8	335	85	0.012	0.11	1	31
9	236.7	41.2	0.0411	0.084	1.41	32
10	275	86	0.0031	0.39	1	33
11	164	211	0.0019	0.465	1.419	34

The effective strain rate for a spindle speed range of 25 rpm to 500 rpm is displayed in Fig. 5. The corresponding deposition temperature-spindle speed relationships for all 11 Johnson-Cook models are shown in Fig. 6. It is observed that the temperature-spindle speed relationships are nonlinear, and the results differ based on the Johnson-Cook model parameters. The mean of all 11 curves from Fig. 6 is displayed in Fig. 7. Results from [23] are also included (red square), where the numerical simulation was performed using an open-source computational fluid dynamics code. Good agreement is observed.

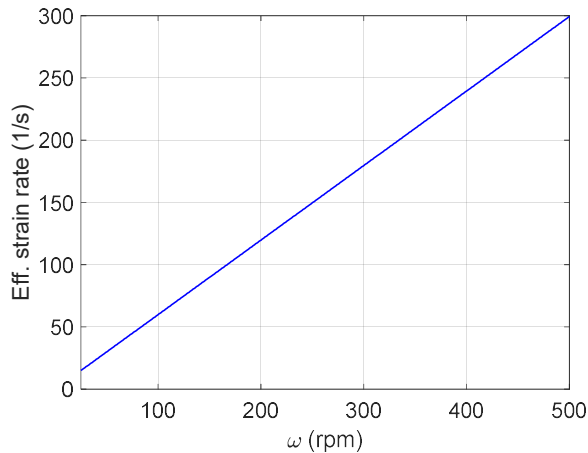


Figure 5: Spindle speed-effective strain rate relationship for selected spindle speed range.

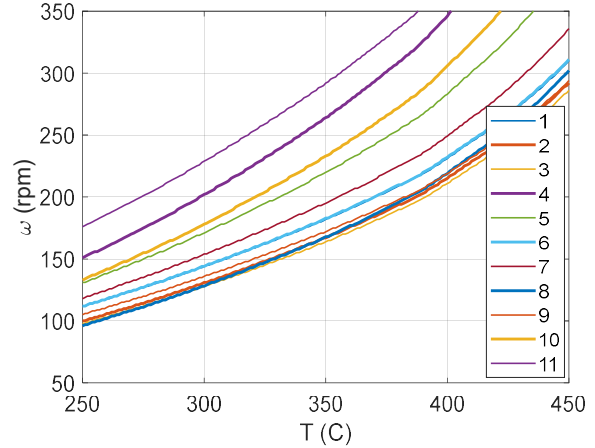


Figure 6: Deposition temperature-spindle speed relationships for 11 different 6061 aluminum Johnson-Cook flow stress models (Table 1) for a temperature range of 250 C to 450 C.

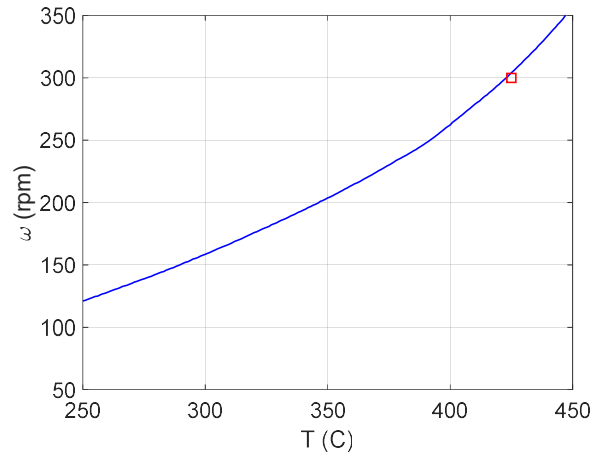


Figure 7: Mean deposition temperature-spindle speed relationship from Fig. 6 (blue line) with numerical simulation result (red square) for 6061 aluminum and the same operating parameters [23].

3. Experimental Setup

Experiments were completed using a MELD Manufacturing L3 machine; see Fig. 8. The L3 is a three-axis computer numerical control (CNC) machine tool with the deposition head mounted to the vertical (z) axis. The AFSD head includes an actuator and pushrod to provide the downward (normal direction) force. The L3 deposits material in discrete sections, where feedstock is loaded into the pushrod-spindle-tool assembly through the tool opening near the table, where the build plate is mounted. After insertion, the 12.7 mm square by 508 mm long feedstock is forced downward through the rotating spindle and tool. The feedstock was 7075 aluminum for this study due to its relevance in aerospace applications.

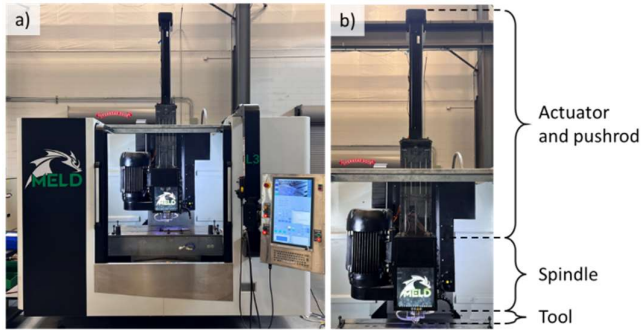


Figure 8: a) MELD Manufacturing L3 AFSD machine. b) Details for actuator and pushrod, spindle, and tool assembly.

The tool can have a flat shoulder face or can contain features to modify the deposition process similar to friction stir welding tool geometries [37–38]. For this study, the 38.1 mm diameter, copper beryllium (CuBe) tool from MELD Manufacturing included a 12.7 mm square bore and an H13 tool steel cap with four 2.3 mm tall teardrop-shaped protrusions located at varying radii from the tool center. The tool also had an embedded K-type thermocouple. It was radially offset from the tool center (outside the square bore) and was located axially 0.25 mm to 0.38 mm from the tool face. The thermocouple was used to measure tool temperature with a sampling frequency of 1 Hz. A module was attached to the rotating spindle which transmitted temperature to the machine controller. This temperature was recorded and could be used for closed-loop control, where the spindle speed is adjusted continuously to maintain a commanded temperature. The closed-loop temperature control is enabled and disabled using appropriate m-codes within the part program. It was disabled for this testing since the intent was to identify the relationship between deposition temperature and a fixed spindle speed. The setup is displayed in Fig. 9, where the external tool cooling jacket is also shown.

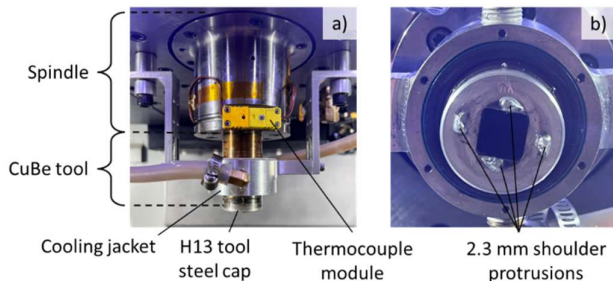


Figure 9: a) CuBe tool with H13 tool steel cap, thermocouple connection, and cooling jacket. b) Bottom view of tool showing shoulder face protrusions and 12.7 mm square feedstock bore.

4. Results

Tests were completed to deposit 7075 aluminum feedstock on a 7075-T651 aluminum build plate at selected spindle speeds. Prior to deposition, the build plate surface was

roughened using fine grit sandpaper and cleaned with isopropyl alcohol. The temperature was measured using the tool thermocouple to compare with model predictions. A single wall build strategy was selected where each layer was deposited on the previous layer. Each layer included a deposition initiation cycle, which was followed by constant parameter deposition. The deposition initiation cycle was implemented to repeatedly reach an increased temperature which permitted the desired plastic flow. It was automated as a subroutine within the multi-layer wall part program.

The deposition initiation cycle for the first layer began with the tool located 1.5 mm above the build surface and a spindle speed of $\omega = 350$ rpm at the desired starting point. The feedstock feed velocity was set to $F = 25.4$ mm/min (time 1 in Fig. 10). These parameters were maintained until the threshold axial force of 4003 N (900 lbf) was reached (time 2); this force was measured using the actuator drive current. The feedstock feed velocity was then reduced to 17.5 mm/min to prevent pushrod overloading until the tool thermocouple temperature threshold of $T = 115$ C was reached (time 3). The spindle speed was reduced to 275 rpm to prevent temperature overshoot at the start of the tool feed across the build plate (or prior layer) surface. The feedstock feed velocity was increased to 28 mm/min to fill the gap between tool and build surface with plastically deformed feedstock. These operating parameters were maintained until the tool temperature reached a final threshold of 370 C (time 4). At this point, the desired constant spindle speed, feedstock feed velocity, and tool feed velocity to be used for deposition were commanded. Note that the feedstock feed velocity values were reduced by 50% in the first layer to ensure successful bonding with the build plate. In all other layers, the feed velocity values listed here were doubled.

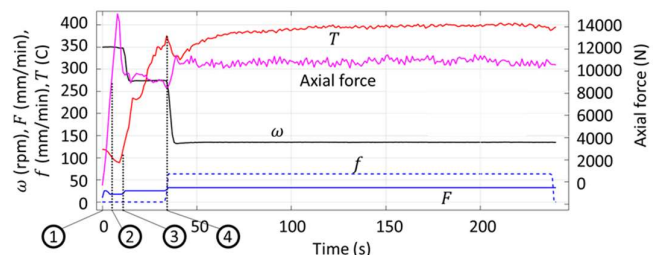


Figure 10: Process signals during first layer deposition. Key times in the first layer deposition initiation cycle are identified: 1) set $\omega = 350$ rpm and $F = 25.4$ mm/min and wait for axial force threshold; 2) axial force of 4003 N reached, reduce F to 17.5 mm/min and wait for threshold temperature; 3) temperature threshold of 115 C reached, reduce ω to 275 rpm and increase F to 28 mm/min, hold until final temperature threshold is reached; and 4) final temperature threshold of 370 C reached, command desired constant spindle speed, feedstock feed velocity, and tool feed velocity.

The full deposition sequence is displayed in Fig. 11a. Starting in the top right, the deposition initiation cycle is the first step. Proceeding counter-clockwise, the first layer was deposited at the desired constant spindle speed, feedstock feed velocity, and tool feed velocity. The layer length was 215.9 mm, the approximate width was 54.1 mm, and the height was 1.5 mm. At the end of the 215.9 mm tool feed length, the feedstock feed was stopped, the tool was retracted by 25.4 mm

in the z direction, and the spindle rotation was stopped. The tool was then returned to the starting location, a two-minute delay was completed, and the deposition initiation cycle was repeated after setting the tool-build surface gap back to 1.5 mm. The process was repeated for 30 layers to reach a final wall height of 45 mm (an example is shown in Fig. 11b).

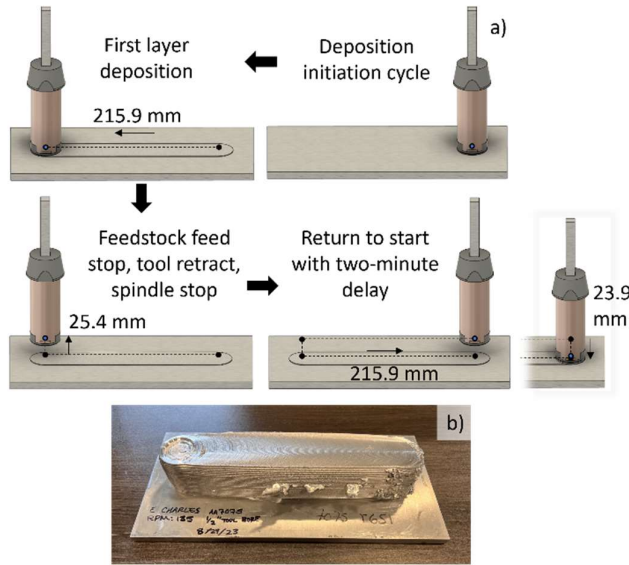


Figure 11: a) Deposition sequence (counter-clockwise from top right). b) Example 7075 aluminum wall geometry with 30 layers.

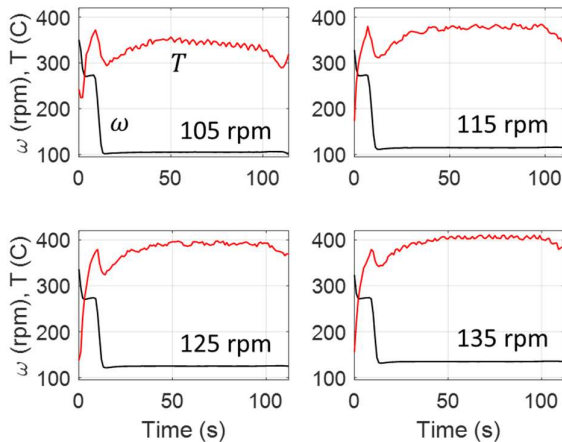


Figure 12: Second layer spindle speed and temperature data for four test cases, where $\omega = \{105, 115, 125, \text{ and } 135\}$ rpm. The initial variation in spindle speed (and corresponding temperature response) is due to the deposition initiation cycle.

Four 30-layer walls were deposited using the following parameters: 1.5 mm layer height, $f = 127$ mm/min, $F = 65$ mm/min, and $\omega = \{105, 115, 125, \text{ and } 135\}$ rpm. The corresponding F/f ratio was 0.51 and the approximate layer width was 54.1 mm. The lower and upper spindle speed limits were selected to avoid exceeding the machine’s axial force and spindle torque limits, while keeping the temperature below the 7075 aluminum solidus of approximately 477 C to avoid incipient melting [39-40]. For comparison to model predictions, the mean steady-state temperature from the second layer was selected because, as noted, each first layer was

deposited at 50% of the commanded feedstock and tool feed velocities for the other layers to enable successful bonding to the build plate. The time-dependent spindle speed (due to the deposition initiation cycle) and corresponding temperature are displayed in Fig. 12 for the four spindle speeds. It is observed that the steady-state deposition temperature increases with the selected (constant) spindle speed, as expected.

The algorithm detailed in the AFSD temperature model section was used to predict the relationship between deposition temperature and spindle speed for 7075 aluminum. The Johnson-Cook model parameters from seven references (nine total models) are listed in Table 2 [41-47]. The temperature-dependent thermal conductivity for 7075 aluminum from Fig. 4 [36] was again used. The friction radius was 13.525 mm (half the deposition radius of 27.05 mm), the friction coefficient was 0.25, the initial temperature was 25 C, and the square feedstock side length was 12.7 mm. The deposition temperature-spindle speed relationship from the nine Johnson-Cook models is shown in Fig. 13.

Table 2: Johnson-Cook model parameters for 7075 aluminum [41-47].

Model	A (MPa)	B (MPa)	C	n	m	T_m (°C)	ϵ_0 (1/s)	Ref.
1	520	477	0.001	0.52	1	619.85	0.0005	40
2	527	575	0.017	0.72	1.61	619.85	1	41
3	546	678	0.024	0.71	1.56	619.85	1	41
4	517	405	0.0075	0.41	1.1	619.85	0.000161	42
5	452.4	457.1	0.01085	0.3572	1.131	619.85	1	43
6	448.454	475.808	0.0012	0.3948	1.29	619.85	0.0001	44
7	665.6	72.6	0.002	0.48	0.79	635	1	45
8	496	310	0	0.41	1.2	635	1	45
9	435.7	534.624	0.019	0.504	0.97	619.85	1	46

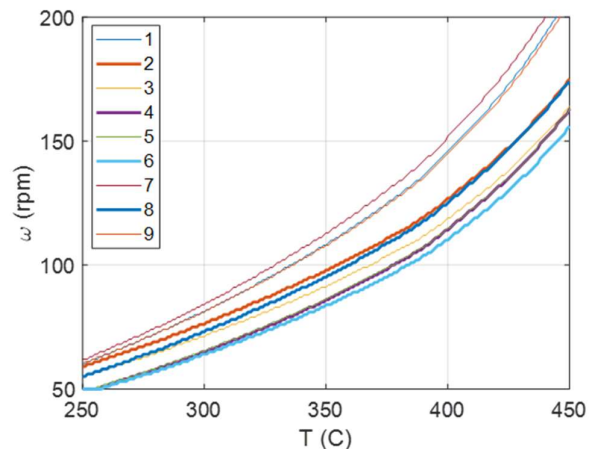


Figure 13: Deposition temperature-spindle speed relationships for nine different 7075 aluminum Johnson-Cook flow stress models (Table 2, [41-47]) for a temperature range of 250 C to 450 C.

The mean of the nine curves in Fig. 13 was used to compare with the four experimental temperature-spindle speed combinations. This comparison between the mean predicted deposition temperature-spindle speed relationship (blue line)

and measured tool temperatures for four spindle speeds (red squares) is displayed in Fig. 14. The execution time for Fig. 14 was 2.225 s (Intel Core i7-8850H CPU, 2.60GHz, 32 GB RAM, MATLAB 2023b). The temperature was obtained from the steady-state portions of the four panels in Fig. 12 (50 s to 70 s). The error bars indicate the 95% confidence intervals (i.e., the standard deviation of the steady-state portion was calculated and the error bars were plotted for \pm two times the standard deviation). Good agreement is observed with overlap of the error bars and prediction in three of four cases.

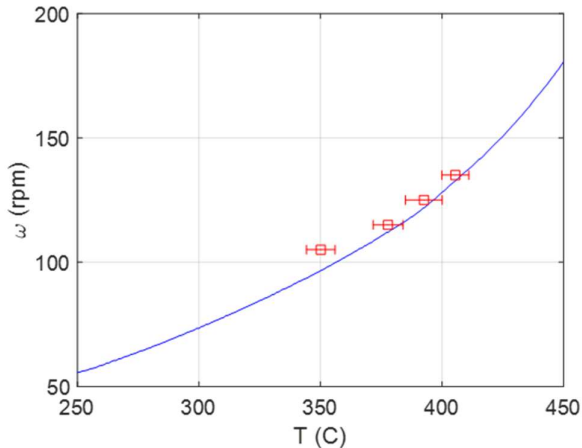


Figure 14: Mean deposition temperature-spindle speed relationship (blue line) with experimental results (red squares) at $\omega = \{105, 115, 125, \text{ and } 135\}$ rpm for 7075 aluminum. The error bars indicate 95% confidence intervals.

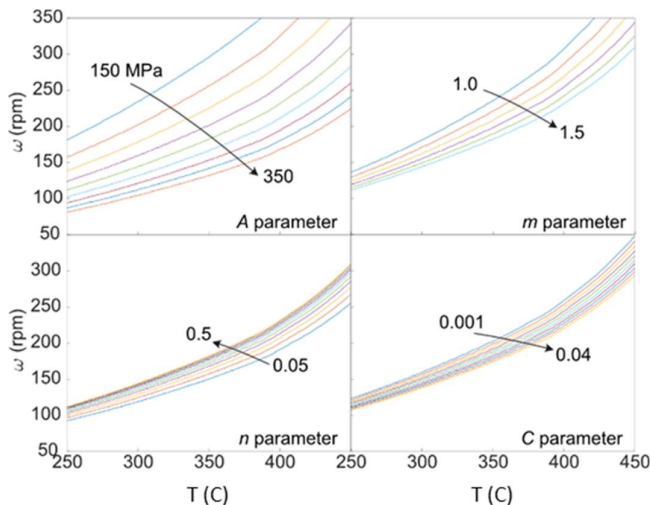


Figure 15: Sensitivity analysis results. The four panels identify the parameter that was individually varied (A , m , C , or n clockwise from top left), the range of the variation, and the distribution in the T - ω relationships for the selected parameter range. The largest sensitivity is observed for the A parameter.

As a final study, a sensitivity analysis was performed to evaluate the dependence of the temperature-spindle speed relationship on the individual parameters in the Johnson-Cook flow stress model. Baseline parameters were selected to be $A = 250$ MPa, $B = 80$ MPa, $C = 0.025$, $n = 0.5$, and $m = 1.5$. The A , C , m , and n parameters were then varied individually (over approximately the range provided in Table 1) with all other parameters set to their baseline values. The results are

displayed in Fig. 15. It is observed that the temperature-spindle speed relationship is most sensitive to the A parameter, which represents the feedstock yield strength identified under quasi-static strain rate conditions. As yield stress increases, the temperature increases for a given spindle speed, since more work is required to deform the material. The effect of increasing the strain hardening exponent, n , may initially appear counter intuitive, in that the model predicts lower temperature with increasing hardening exponent. However, this is because, in the Johnson-Cook model, when all other parameters are held constant, increasing the strain hardening exponent *decreases* the initial yield stress in addition to increasing the strain hardening. The B parameter was also investigated, but is not shown because the results of the model are comparably insensitive to variations in the B parameter over the range used for 6061 aluminum (Table 1).

5. Conclusions

This paper detailed a physics-based, analytical model for additive friction stir deposition (AFSD) spindle speed selection to achieve a desired deposition temperature. This predictive capability advances AFSD implementation by improving on the current parameter selection approach based on prior experience or trial and error. Key elements of the model included:

- power input to the feedstock was related to the material temperature rise (and corresponding flow stress reduction) using Fourier's conduction rate equation
- power input was modeled as frictional heating at the deposit-build surface and adiabatic heating due to plastic deformation within the deposit
- the effective strain rate was calculated using the kinematics of the rotating-translating tool motion, the gradient of velocity, the strain rate tensor, and the corresponding strain rate; inputs included the tool rotating speed (spindle speed), tool feed velocity, and friction radius (taken to be half the deposition radius)
- flow stress was predicted using the strain, strain rate, and temperature-dependent Johnson-Cook constitutive model, where multiple sets of model coefficients were used to establish independent temperature-spindle speed relationships and these were then averaged to obtain the final predictive model
- an algorithm was described that included: 1) selecting a deposition temperature (based on the feedstock alloy); 2) defining the temperature-dependent thermal conductivity; 3) calculating the effective strain rate using a pre-selected spindle speed range; 4) calculating the flow stress for the same spindle speed range; 5) evaluating a spindle speed-dependent test function obtained from Fourier's conduction rate equation for the same spindle speed range; 6) determining the function zero crossing and identifying the corresponding spindle speed; 7) recording the temperature-spindle speed pair; and 8) repeating steps 1-7 for the next deposition temperature.

Model predictions were compared to: 1) literature results

from a numerical AFSD simulation using 6061 aluminum feedstock [23]; and 2) AFSD experiments completed using 7075 aluminum feedstock. Good agreement was obtained in both cases using the same modeling approach. A sensitivity analysis for Johnson-Cook flow stress model parameters was also provided.

Limitations for the model include simplifications applied to enable an analytical solution, such as the simplified treatment of friction (dry sliding only). Next steps will include additional comparison to experimental results and improvements of the model.

Acknowledgements

Support for this research was provided by DEVCOM Army Research Laboratory under grant no. W911NF2120020. This work was also supported by the DOE Office of Energy Efficiency and Renewable Energy (EERE), Advanced Manufacturing Office (AMO), under contract DE-AC05-00OR22725. The US government retains and the publisher, by accepting the article for publication, acknowledges that the US government retains a nonexclusive, paid-up, irrevocable, worldwide license to publish or reproduce the published form of this manuscript, or allow others to do so, for US government purposes. DOE will provide public access to these results of federally sponsored research in accordance with the DOE Public Access Plan (<http://energy.gov/downloads/doe-public-access-plan>). The authors also acknowledge support from the NSF Engineering Research Center for Hybrid Autonomous Manufacturing Moving from Evolution to Revolution (ERC-HAMMER) under Award Number EEC-2133630.

References

- [1] Hang, Z.Y., Jones, M.E., Brady, G.W., Griffiths, R.J., Garcia, D., Rauch, H.A., Cox, C.D. and Hardwick, N., 2018. Non-beam-based metal additive manufacturing enabled by additive friction stir deposition. *Scripta Materialia*, 153, pp.122-130.
- [2] Khodabakhshi, F. and Gerlich, A.P., 2018. Potentials and strategies of solid-state additive friction-stir manufacturing technology: A critical review. *Journal of Manufacturing Processes*, 36, pp.77-92.
- [3] Yu, H.Z. and Mishra, R.S., 2021. Additive friction stir deposition: a deformation processing route to metal additive manufacturing. *Materials Research Letters*, 9(2), pp.71-83.
- [4] Gopan, V., Wins, K.L.D. and Surendran, A., 2021. Innovative potential of additive friction stir deposition among current laser based metal additive manufacturing processes: A review. *CIRP Journal of Manufacturing Science and Technology*, 32, pp.228-248.
- [5] Peter Martin, L., Luccitti, A. and Walluk, M., 2022. Evaluation of additive friction stir deposition for the repair of cast Al-1.4 Si-1.1 Cu-1.5 Mg-2.1 Zn. *Journal of Manufacturing Science and Engineering*, 144(6), p.061006.
- [6] Hang, Z.Y., 2022. *Additive Friction Stir Deposition*. Elsevier.
- [7] Mishra, R.S., Haridas, R.S. and Agrawal, P., 2022. Friction stir-based additive manufacturing. *Science and Technology of Welding and Joining*, 27(3), pp.141-165.
- [8] Priedeman, J.L., Phillips, B.J., Lopez, J.J., Tucker Roper, B.E., Hornbuckle, B.C., Darling, K.A., Jordon, J.B., Allison, P.G. and Thompson, G.B., 2020. Microstructure development in additive friction stir-deposited Cu. *Metals*, 10(11), p.1538.
- [9] Perry, M.E., Griffiths, R.J., Garcia, D., Sietins, J.M., Zhu, Y. and Hang, Z.Y., 2020. Morphological and microstructural investigation of the non-planar interface formed in solid-state metal additive manufacturing by additive friction stir deposition. *Additive Manufacturing*, 35, p.101293.
- [10] Griffiths, R.J., Garcia, D., Song, J., Vasudevan, V.K., Steiner, M.A., Cai, W. and Hang, Z.Y., 2021. Solid-state additive manufacturing of aluminum and copper using additive friction stir deposition: Process-microstructure linkages. *Materialia*, 15, p.100967.
- [11] Agrawal, P., Haridas, R.S., Yadav, S., Thapliyal, S., Gaddam, S., Verma, R. and Mishra, R.S., 2021. Processing-structure-property correlation in additive friction stir deposited Ti-6Al-4V alloy from recycled metal chips. *Additive Manufacturing*, 47, p.102259.
- [12] Phillips, B.J., Mason, C.J.T., Beck, S.C., Avery, D.Z., Doherty, K.J., Allison, P.G. and Jordon, J.B., 2021. Effect of parallel deposition path and interface material flow on resulting microstructure and tensile behavior of Al-Mg-Si alloy fabricated by additive friction stir deposition. *Journal of Materials Processing Technology*, 295, p.117169.
- [13] Perry, M.E., Rauch, H.A., Griffiths, R.J., Garcia, D., Sietins, J.M., Zhu, Y., Zhu, Y. and Hang, Z.Y., 2021. Tracing plastic deformation path and concurrent grain refinement during additive friction stir deposition. *Materialia*, 18, p.101159.
- [14] Williams, M.B., Robinson, T.W., Williamson, C.J., Kinser, R.P., Ashmore, N.A., Allison, P.G. and Jordon, J.B., 2021. Elucidating the effect of additive friction stir deposition on the resulting microstructure and mechanical properties of magnesium alloy WE43. *Metals*, 11(11), p.1739.
- [15] Mukhopadhyay, A. and Saha, P., 2022. A critical review on process metrics–microstructural evolution–process performance correlation in additive friction stir deposition (AFS-D). *Journal of the Brazilian Society of Mechanical Sciences and Engineering*, 44(9), p.422.
- [16] Joshi, S.S., Sharma, S., Radhakrishnan, M., Pantawane, M.V., Patil, S.M., Jin, Y., Yang, T., Riley, D.A., Banerjee, R. and Dahotre, N.B., 2022. A multi modal approach to microstructure evolution and mechanical response of additive friction stir deposited AZ31B Mg alloy. *Scientific Reports*, 12(1), p.13234.
- [17] Zeng, C., Ghadimi, H., Ding, H., Nemati, S., Garbie, A., Raush, J. and Guo, S., 2022. Microstructure evolution of Al6061 alloy made by additive friction stir deposition. *Materials*, 15(10), p.3676.

- [18] Kincaid, J., Charles, E., Garcia, R., Dvorak, J., No, T., Smith, S. and Schmitz, T., 2023. Process planning for hybrid manufacturing using additive friction stir deposition. *Manufacturing Letters*, 37, pp.26-31.
- [19] Schmitz, T., Costa, L., Canfield, B.K., Kincaid, J., Zamoski, R., Garcia, R., Frederick, C., Rossy, A.M. and Moeller, T.M., 2023. Embedded QR code for part authentication in additive friction stir deposition. *Manufacturing Letters*, 35, pp.16-19.
- [20] Dvorak, J., Cornelius, A., Corson, G., Zamoski, R., Jacobs, L., Penney, J. and Schmitz, T., 2022. A machining digital twin for hybrid manufacturing. *Manufacturing Letters*, 33(Supplement).
- [21] Cornelius, A., Jacobs, L., Lamsey, M., McNeil, L., Hamel, W. and Schmitz, T., 2022. Hybrid manufacturing of Invar mold for carbon fiber layup using structured light scanning. *Manufacturing letters*, 33(2).
- [22] Cornelius, A., Dvorak, J., Jacobs, L., Penney, J. and Schmitz, T., 2021. Combination of structured light scanning and external fiducials for coordinate system transfer in hybrid manufacturing. *Journal of Manufacturing Processes*, 68, pp.1824-1836.
- [23] Kincaid, K.C., MacPhee, D.W., Stubblefield, G.G., Jordon, J.B., Rushing, T.W. and Allison, P.G., 2023. A finite volume framework for the simulation of additive friction stir deposition. *Journal of Engineering Materials and Technology*, 145(3), p.031002.
- [24] Gotawala, N. and Hang, Z.Y., 2023. Material flow path and extreme thermomechanical processing history during additive friction stir deposition. *Journal of Manufacturing Processes*, 101, pp.114-127.
- [25] Tlusty, G., 2000. *Manufacturing Processes and Equipment*, Prentice Hall, Upper Saddle River, NJ.
- [26] Farren, W.S. and Taylor, G.I., 1925. The heat developed during plastic extension of metals. *Proceedings of the Royal Society of London. Series A, Containing Papers of a Mathematical and Physical Character*, 107(743), pp.422-451.
- [27] Taylor, G.I. and Quinney, H., 1934. The latent energy remaining in a metal after cold working. *Proceedings of the Royal Society of London. Series A, Containing Papers of a Mathematical and Physical Character*, 143(849), pp.307-326.
- [28] Akram, S., Jaffery, S.H.I., Khan, M., Fahad, M., Mubashar, A. and Ali, L., 2018. Numerical and experimental investigation of Johnson–Cook material models for aluminum (Al 6061-T6) alloy using orthogonal machining approach. *Advances in Mechanical Engineering*, 10(9), p.1687814018797794.
- [29] Adibi-Sedeh, A.H., Madhavan, V. and Bahr, B., 2003. Extension of Oxley's analysis of machining to use different material models. *J. Manuf. Sci. Eng.*, 125(4), pp.656-666.
- [30] Boldyrev, I.S., Shchurov, I.A. and Nikonov, A.V., 2016. Numerical simulation of the aluminum 6061-T6 cutting and the effect of the constitutive material model and failure criteria on cutting forces' prediction. *Procedia Engineering*, 150, pp.866-870.
- [31] Daoud, M., Jomaa, W., Chatelain, J.F. and Bouzid, A., 2015. A machining-based methodology to identify material constitutive law for finite element simulation. *The International Journal of Advanced Manufacturing Technology*, 77, pp.2019-2033.
- [32] Daoud, M., Jomaa, W., Chatelain, J.F., Bouzid, A. and Songmene, V., 2014. Identification of material constitutive law constants using machining tests: A response surface methodology based approach. *WIT Transactions on The Built Environment*, 137, pp.25-36.
- [33] Fernandez-Zelaia, P. and Melkote, S.N., 2019. Statistical calibration and uncertainty quantification of complex machining computer models. *International Journal of Machine Tools and Manufacture*, 136, pp.45-61.
- [34] Pittalà, G.M. and Monno, M., 2010. 3D finite element modeling of face milling of continuous chip material. *The International Journal of Advanced Manufacturing Technology*, 47, pp.543-555.
- [35] Rule, W.K., 1997. A numerical scheme for extracting strength model coefficients from Taylor test data. *International Journal of Impact Engineering*, 19(9-10), pp.797-810.
- [36] He, M., Zhang, Z., Mao, W., Li, B., Bai, Y. and Xu, J., 2019. Numerical and experimental study on melt treatment for large-volume 7075 alloy by a modified annular electromagnetic stirring. *Materials*, 12(5), p.820.
- [37] Vairis, A., Petousis, M., Mountakis, N., Tsarouchidou, C. and Vidakis, N. 2022. The effect of tool geometry on the strength of FSW aluminum thin sheets. *Materials*, 15(22), p.8187.
- [38] Hattingh, D., Blignault, C., van Niekerk, T. and James, M., 2008. Characterization of the influences of FSW tool geometry on welding forces and weld tensile strength using an instrumented tool. *J Mater Process Technol*, 203(1-3), pp.46-57.
- [39] Brehm, J., Buckner, J., Profazi, C. and Hickman, A., 2022. Incipient melting in AA7075 (SAND2022-9908). Sandia National Lab. (SNL-NM), Albuquerque, NM (United States).
- [40] Zou, X., Yan, H. and Chen, X., 2017. Evolution of second phases and mechanical properties of 7075 Al alloy processed by solution heat treatment. *Transactions of Nonferrous Metals Society of China (English Edition)*, 27(10), pp.2146-2155.
- [41] Aslam, M.A., Ke, Z., Rayhan, S.B., Faizan, M. and Bello, I.M., 2020, November. An investigation of soft impacts on selected aerospace grade alloys based on Johnson-Cook Material Model. In *Journal of Physics: Conference Series* (Vol. 1707, No. 1, p. 012008). IOP Publishing.
- [42] Brar, N.S., Joshi, V.S. and Harris, B.W., 2009, December. Constitutive model constants for Al7075-T651 and Al7075-T6. In *AIP conference proceedings* (Vol. 1195, No. 1, pp. 945-948). American Institute of Physics.
- [43] Corona, E. and Orient, G.E., 2014. An evaluation of the Johnson-Cook model to simulate puncture of 7075 aluminum plates (No. SAND2014-1550). Sandia National Lab. (SNL-NM), Albuquerque, NM (United States).

- [44] Rule, W.K. and Jones, S.E., 1998. A revised form for the Johnson-Cook strength model. *International Journal of Impact Engineering*, 21(8), pp.609-624.
- [45] Senthil, K., Iqbal, M.A., Chandel, P.S. and Gupta, N.K., 2017. Study of the constitutive behavior of 7075-T651 aluminum alloy. *International Journal of Impact Engineering*, 108, pp.171-190.
- [46] Wang, Z., Cao, Y., Gorbachev, S., Kuzin, V., He, W. and Guo, J., 2022. Research on conventional and high-speed machining cutting force of 7075-T6 aluminum alloy based on finite element modeling and simulation. *Metals*, 12(8), p.1395.
- [47] Zhang, P., Liu, J., Gao, Y., Liu, Z. and Mai, Q., 2023. Effect of heat treatment process on the micro machinability of 7075 aluminum alloy. *Vacuum*, 207, p.111574.